

Tunable Pseudocapacitance in 3D $\text{TiO}_{2-\delta}$ Nanomembranes Enabling Superior Lithium Storage Performance

Shaozhuan Huang,^{*,†,‡} Lin Zhang,^{*,†} Xueyi Lu,[†] Lifeng Liu,^{‡,§} Lixiang Liu,[†] Xiaolei Sun,^{†,§} Yin Yin,[†] Steffen Oswald,^{||} Zhaoyong Zou,[§] Fei Ding,[†] and Oliver G. Schmidt^{†,⊥}

[†]Institute for Integrative Nanosciences and ^{||}Institute for Complex Materials, IFW Dresden, Helmholtzstraße 20, Dresden 01069, Germany

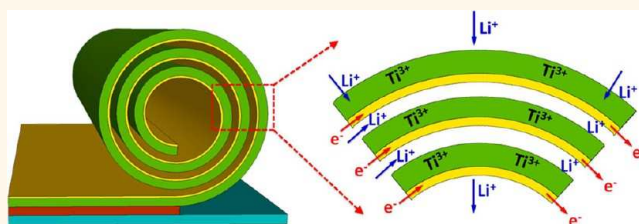
[‡]International Iberian Nanotechnology Laboratory (INL), Avenida Mestre Jose Veiga, 4715-330, Braga, Portugal

[§]Department of Biomaterials, Max Planck Institute of Colloids and Interfaces, Potsdam 14424, Germany

[⊥]Material Systems for Nanoelectronics, Technische Universität Chemnitz, Chemnitz, Germany

S Supporting Information

ABSTRACT: Nanostructured TiO_2 of different polymorphs, mostly prepared by hydro/solvothermal methods, have been extensively studied for more than a decade as anode materials in lithium ion batteries. Enormous efforts have been devoted to improving the electrical conductivity and lithium ion diffusivity in chemically synthesized TiO_2 nanostructures. In this work we demonstrate that 3D Ti^{3+} -self-doped TiO_2 ($\text{TiO}_{2-\delta}$) nanomembranes, which are prepared by physical vapor deposition combined with strain-released rolled-up technology, have a great potential to address several of the long-standing challenges associated with TiO_2 anodes. The intrinsic electrical conductivity of the TiO_2 layer can be significantly improved by the *in situ* generated Ti^{3+} , and the amorphous, thin TiO_2 nanomembrane provides a shortened Li^+ diffusion pathway. The fabricated material shows a favorable electrochemical reaction mechanism for lithium storage. Further, post-treatments are employed to adjust the Ti^{3+} concentration and crystallinity degree in TiO_2 nanomembranes, providing an opportunity to investigate the important influences of Ti^{3+} self-doping and amorphous structures on the electrochemical processes. With these experiments, the pseudocapacitance contributions in TiO_2 nanomembranes with different crystallinity degree are quantified and verified by an in-depth kinetics analysis. Additionally, an ultrathin metallic Ti layer can be included, which further improves the lithium storage properties of the TiO_2 , giving rise to the state-of-the-art capacity (200 mAh g^{-1} at 1 C), excellent rate capability (up to 50 C), and ultralong lifetime (for 5000 cycles at 10 C, with an extraordinary retention of 100%) of TiO_2 anodes.



KEYWORDS: 3D nanomembrane, titanium dioxide, Ti^{3+} self-doping, tunable pseudocapacitance, lithium ion battery

Lithium ion batteries (LIBs) are among the leading energy storage systems and have attracted substantial research efforts in recent years.^{1–3} A major challenge for LIBs is to develop electrode materials with high energy density, excellent rate capability, and long cycle life to meet the demand for ever-increasing energy/power densities.⁴ Recently, titanium dioxide (TiO_2) has attracted much attention, because it is a low-cost and environmentally benign material. TiO_2 is structurally and electrochemically stable during charge/discharge processes, and it can avoid lithium electroplating, which causes safety concerns.^{5,6} However, the poor rate capability and long-term performance of TiO_2 electrodes, which are caused by the limited Li^+ diffusivity and electrical conductivity,⁷ severely hinder their practical applications.

Nanostructured TiO_2 is appealing in this regard because it can provide large electrode/electrolyte contact areas and improve Li^+ ion transport in the electrode by shortening the Li^+ diffusion pathway. The electrical conductivity can be improved by compositing/doping TiO_2 with conductive alien species. To date, TiO_2 anatase, rutile, and bronze polymorph anodes with various nanostructures have been synthesized mostly by hydro/solvothermal methods. Despite many successful reports, major challenges remain in LIB research with these designed materials:⁸ (i) The TiO_2 electrode

Received: October 28, 2016

Accepted: December 27, 2016

Published: December 27, 2016

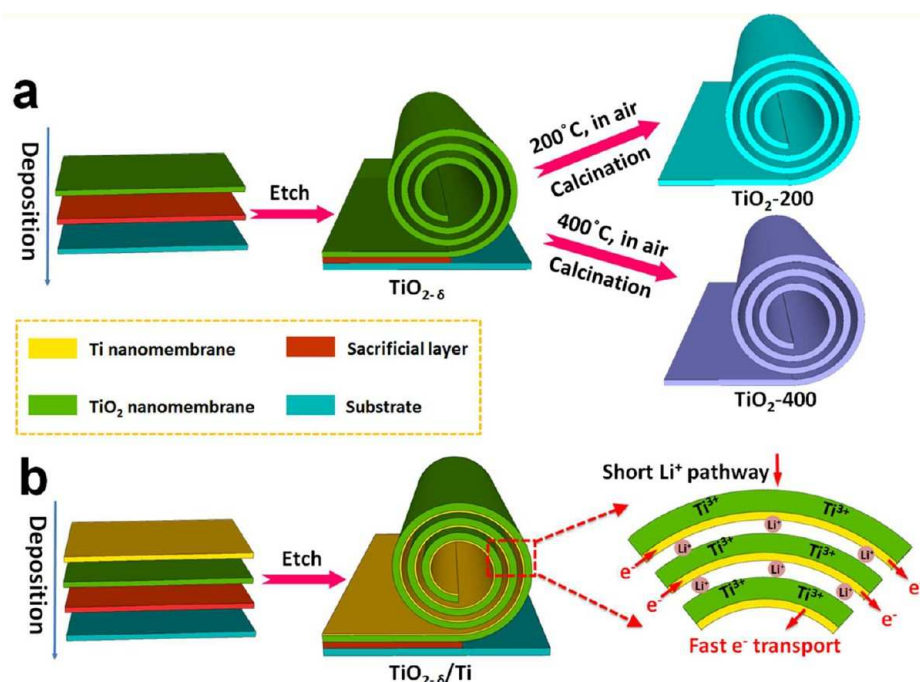


Figure 1. (a) Schematic illustration of the fabrication process of the rolled-up TiO_{2-δ}, TiO₂-200, and TiO₂-400 nanomembranes. (b) Schematic illustration of the fabrication process of a rolled-up TiO_{2-δ}/Ti bilayer nanomembranes and their electrochemical reaction mechanism: the Ti³⁺ and metallic Ti network improve the electrical conductivity; the ultrathin nanomembranes and the channels between the layer windings provide shortened pathways for superfast Li⁺ diffusion. The structural integrity after long-term cycling is guaranteed by the flexible thin membrane in the tubular configuration.

performance, which differs significantly from one report to another, depends on the size, morphology, crystallinity, and even purity of the material, thus rendering a systematic study on the lithium storage mechanism very difficult. (ii) Doping with alien species (e.g., carbon⁹ and nitrogen¹⁰) can cause impurity defects and thermal instability.¹¹ Ti³⁺ self-doping is an alternative strategy to enhance the inherent electrical conductivity of TiO₂,^{12–16} but it is mainly carried out under high-temperature annealing of nanostructured powders in a reducing atmosphere, which is unsafe and detrimental to the structural integrity. (iii) In most cases the aggregation of nanostructured TiO₂ is a severe problem, which limits the Li⁺ ion transport from the interior of the electrode to the electrolyte and degrades the lithium storage at high cycling rates. Porous/hollow TiO₂ nanostructures can partly alleviate this issue, but their long-term structural stability still needs to be improved.¹⁷

To tackle these challenges, we introduce a 3D TiO_{2-δ} nanomembrane anode, which is fabricated by physical vapor deposition combined with strain-released rolled-up technology (Figure 1).¹⁸ The rational design of this material is based on the following considerations: (i) The physical vapor deposition is a facile method to obtain amorphous TiO₂ layers with a high controllability and reproducibility. Legrain *et al.*¹⁹ suggested that amorphous TiO₂ may be the most favorable phase for Li⁺ insertion compared to its crystalline counterparts. The amorphous phase provides insertion sites well-distributed in energies, with the lowest energy site being even more favorable than that of TiO₂-B by almost 1 eV for Li⁺. Also, its disordered structure contributes significant pseudocapacitance to the total capacity, resulting in improved rate capabilities and Li⁺ diffusion coefficients.^{20–22} (ii) Ti³⁺ is *in situ* generated through controlling the oxygen pressure in the deposition process and

dispersed uniformly in the whole structure. This important feature is not easily achievable with hydro/solvothermal methods. After the growth, calcinations of TiO_{2-δ} can be performed in a controllable manner (Figure 1a), allowing for a systematic investigation of the influences of different Ti³⁺ doping levels. (iii) Additionally a metallic Ti layer can be included, which serves as a mechanically stable, electrochemically inactive, and electrical conductive 3D network (Figure 1b) to enhance the electrical conductivity. (iv) The problem of nanomaterial aggregation can be avoided. The channels between the layer windings (Figure 1b) allow the penetration of electrolyte into the interior of the electrode and increase the electrode/electrolyte contact area for superfast Li⁺ diffusion. Unlike most porous/hollow TiO₂ nanostructures, the flexible nanomembranes exhibit superior mechanical stability for long lifetime cycling. A synergy of these design routes endows the 3D TiO_{2-δ} nanomembrane electrodes with enhanced pseudocapacitive contributions, superfast Li⁺ diffusion, highly efficient electron transport, and excellent stress relaxation, giving rise to prominent lithium storage performance.

RESULTS AND DISCUSSION

The typical fabrication procedure of TiO₂ nanomembranes is illustrated in Figure 1a. Briefly, photoresist as a sacrificial layer is first spin-coated onto the substrate; then TiO₂ layers are deposited with high controllability (regarding thickness, composition, stacking sequence, *etc.*) onto the sacrificial layer by electron beam evaporation under controllable oxygen atmosphere, during which the intrinsic strain is generated.²³ Finally, the 2D nanomembranes naturally roll up into 3D tubular structures by releasing the intrinsic strain after dissolving the sacrificial layer. With no intentional heating of the substrate, the pristine TiO₂ nanomembranes are

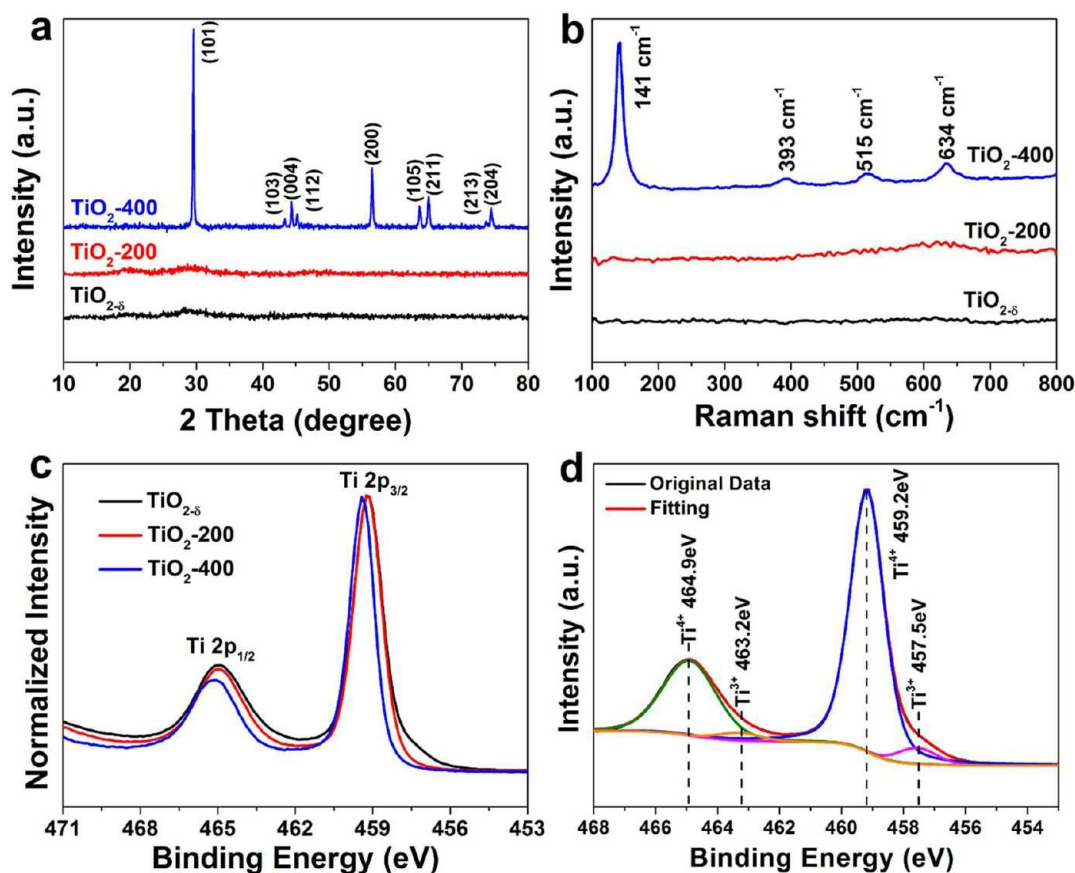


Figure 2. Structural characterization of the pristine TiO_{2-δ}, TiO₂-200, and TiO₂-400 nanomembranes: (a) XRD patterns, (b) Raman spectra, (c) XPS spectra of Ti 2p, (d) XPS spectrum of Ti 2p for TiO_{2-δ}.

amorphous. This has been confirmed by X-ray diffraction (XRD) pattern (Figure 2a) and Raman spectrum (Figure 2b), where no clear peaks associated with crystalline TiO₂ are observed.²⁴ Through adjusting the oxygen concentration, TiO₂ nanomembranes with different oxidation degrees can be realized. On the one hand, the pressure of the deposition chamber must be lower than 1.5×10^{-4} mbar in electron beam deposition to allow passage of electrons from the electron gun to the evaporation material;²⁵ on the other hand, too low oxygen concentration will produce too high oxygen deficiency, which reduces the total number of redox-active Ti⁴⁺. Therefore, in this work, a rational oxygen pressure of 1.4×10^{-4} mbar was used to produce TiO₂ layers having rational Ti³⁺ and oxygen vacancies throughout the whole product (which are denoted as TiO_{2-δ}). The generated Ti³⁺ and oxygen vacancies donate excess unpaired electrons to the structure and therefore enhance the surface reactivity.^{14,26} The oxidation process can be written as $\text{Ti} + \text{O}_2 \rightarrow \text{TiO}_2 + \text{O}_v + \delta\text{Ti}^{3+} + \gamma\text{O}^{2-}$. The existence of Ti³⁺ is confirmed by X-ray photoelectron spectroscopy (XPS), as depicted in Figure 2c and d. Figure 2d shows the core-level XPS spectrum of Ti 2p from the TiO_{2-δ} sample, in which the two major peaks at 459.2 and 464.9 eV correspond to the typical Ti⁴⁺ 2p_{3/2} and Ti⁴⁺ 2p_{1/2} peaks, respectively. Besides, the two shoulder peaks at 457.5 and 463.3 eV are attributed to Ti³⁺ 2p_{3/2} and Ti³⁺ 2p_{1/2}, confirming the presence of Ti³⁺ in TiO_{2-δ} nanomembranes. This result is in agreement with previous reports on TiO_{2-δ} obtained *via* chemical synthesis.^{16,27,28} Such a shoulder could not be observed in stoichiometric TiO₂. A significant advantage of this method is that the Ti³⁺ species are generated during the

whole fabrication process and are uniformly dispersed throughout the entire TiO₂ layer, not just on the surface. According to the thermogravimetric/differential scanning calorimetry (TG/DSC) analysis, the oxygen deficiency of the TiO_{2-δ} is calculated to be 5.31–7.66% (Figure S1).

To reveal the influences of different Ti³⁺ doping levels, a postannealing process is employed to adjust the crystallinity degree and Ti³⁺ concentration in TiO₂ nanomembranes. Two samples denoted as TiO₂-200 and TiO₂-400 are obtained by postheating the pristine TiO_{2-δ} samples in air at 200 and 400 °C, respectively. As for TiO₂-200, no peaks belonging to anatase TiO₂ are observed in both the XRD pattern (Figure 2a, middle) and Raman spectrum (Figure 2b, middle), consistent with the observations for the pristine sample, indicating the poor crystallinity of TiO₂-200 nanomembranes. Despite the negligible changes in crystallinity, the calcination process oxidizes the Ti³⁺ to Ti⁴⁺ and reduces oxygen deficiencies in TiO₂-200. As confirmed in Figure 2c, the shoulder peaks associated with Ti³⁺ disappear, indicating the oxidation of Ti³⁺ to Ti⁴⁺ in TiO₂-200. After annealing at 400 °C, the amorphous TiO₂ is converted to anatase phase (TiO₂-400), as shown in Figure 2a and b. In the XRD pattern, all the reflections of TiO₂-400 nanomembranes are in good agreement with the standard pattern of tetragonal anatase TiO₂ (JCPDS card no. 84-1286). Also, the TiO₂-400 exhibits typical Raman modes of anatase TiO₂ (Figure 2b).²⁹ Together with the significant changes in crystallinity, the calcination process oxidizes the Ti³⁺ to Ti⁴⁺ completely in TiO₂-400, which is evidenced by the two characteristic peaks related to Ti⁴⁺ in the XPS spectrum (Figure 2c).

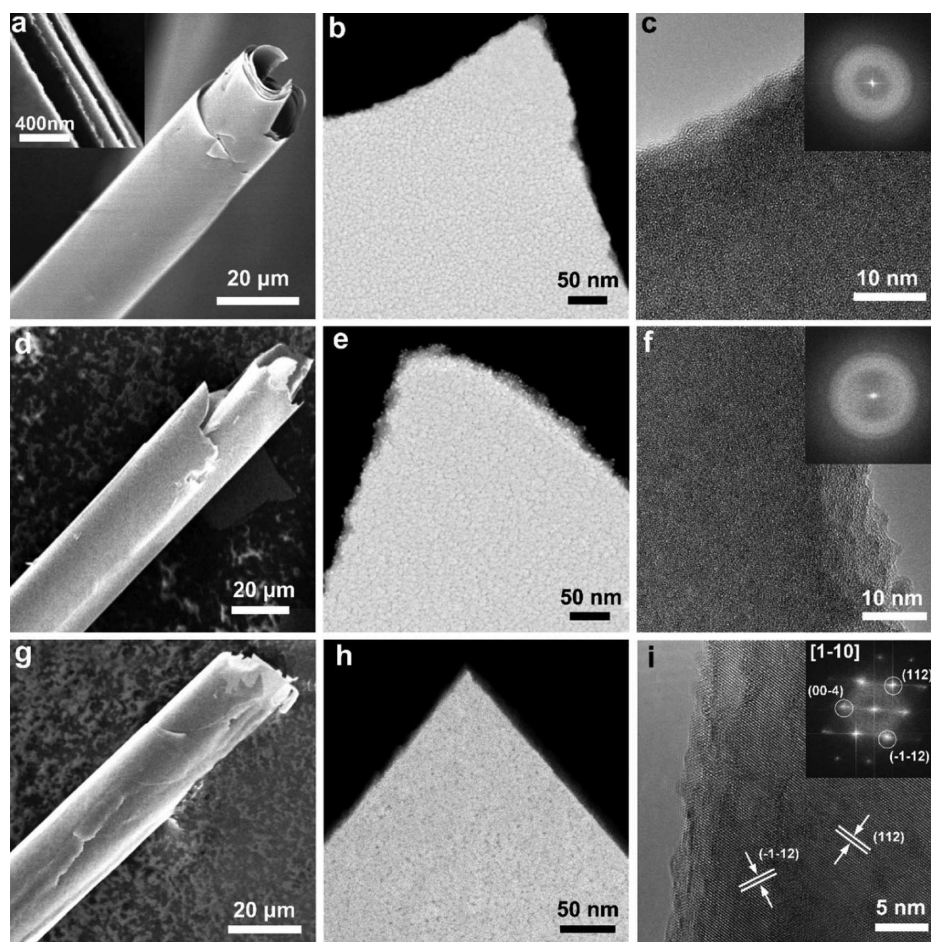


Figure 3. Morphology and structure characterizations of $\text{TiO}_{2-\delta}$ (a–c), TiO_{2-200} (d–f), and TiO_{2-400} (g–i). (a, d, g) SEM images, (b, e, h) HAADF-STEM images, (c, f, i) HRTEM images. Insets in (c), (f), and (i) are the corresponding FFT patterns.

The morphology and structure of the $\text{TiO}_{2-\delta}$, TiO_{2-200} , and TiO_{2-400} are characterized by scanning electron microscopy (SEM) and transmission electron microscopy (TEM) techniques (Figure 3). The low-magnification SEM image (Figure S3) shows that the $\text{TiO}_{2-\delta}$ nanomembranes roll up into 3D microtubes with an average diameter of around 20 μm . Figure 3a shows the morphology of a single microtube, where the open tube end can be clearly seen. A high-magnification SEM image (inset in Figure 3a) further reveals the multiple windings of a microtube with single-layer thickness of a few tens of nanometers. The channels between the windings improve the electrode/electrolyte contact area and shorten the Li^+ diffusion pathway. The high-angle annular dark-field scanning TEM (HAADF-STEM) image (Figure 3b) clearly reveals that the $\text{TiO}_{2-\delta}$ nanomembrane consists of a large number of nanoparticles and many voids exist between the particle boundaries, which can further enhance the lithium storage kinetics due to the shortened Li^+ diffusion pathway and improved Li^+ storage active sites. The interface voids between the nanoparticles are also verified by the overfocus TEM image (Figure S4), where the bright image contrast at overfocus condition is evident along the particle boundaries.³⁰ The high-resolution TEM (HRTEM) image (Figure 3c) and the corresponding fast Fourier transform (FFT) pattern confirm the amorphous nature of $\text{TiO}_{2-\delta}$ nanomembranes. After the calcination processes at 200 and 400 $^{\circ}\text{C}$, there is no significant change in the tubular morphologies of TiO_{2-200} and TiO_{2-400}

(Figure 3d and g). The nanomembranes are rough and composed of many interconnected nanoparticles (Figure 3e and h). Consistent with the XRD pattern, the TiO_{2-200} exhibits no crystalline feature (Figure 3f), while for TiO_{2-400} , well-resolved lattice fringes with spacings of 0.233 nm can be clearly observed, corresponding to the lattice distance of (112) and ($-1-12$) planes, respectively (Figure 3i). Further, the inset FFT shows a well-defined spotted pattern corresponding to the diffractions along the $[1-10]$ zone axis. The SEM-EDS (Figure S5) and STEM-EDS (Figure S6) elemental mapping images of the three samples demonstrate the uniform distribution of Ti and O elements through each sample.

In order to compare the lithium storage performances of $\text{TiO}_{2-\delta}$, TiO_{2-200} , and TiO_{2-400} electrodes, lithium batteries with metallic Li as counter and reference electrode are assembled and tested in the electrochemical windows of 1–3 V, as shown in Figure 4. The electrochemical Li^+ insertion/extraction process is represented by the following equation:^{31,32}



where x is varied with different TiO_2 polymorphs, morphology, and crystalline degree. Figure 4a–c show the galvanostatic discharge–charge profiles of $\text{TiO}_{2-\delta}$, TiO_{2-200} , and TiO_{2-400} nanomembranes at different cycles at 1 C rate. For both $\text{TiO}_{2-\delta}$ and TiO_{2-200} , there are no distinct plateaus in the discharge–charge profiles, implying the amorphous nature of TiO_2 in these samples. This phenomenon has been observed previously

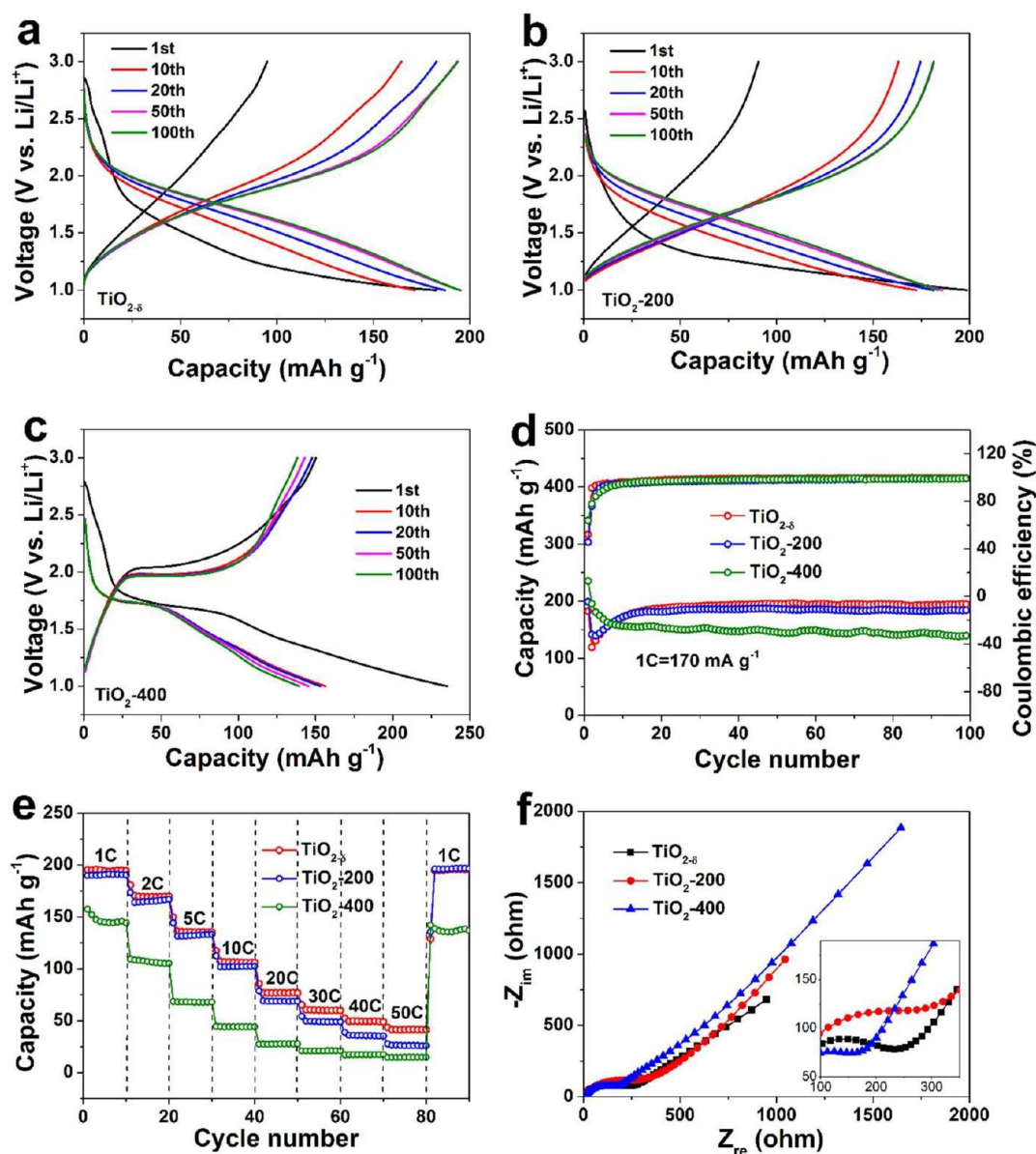


Figure 4. Electrochemical performances of TiO_{2-δ}, TiO₂-200, and TiO₂-400: charge–discharge profiles at 1 C (170 mA g⁻¹) of TiO_{2-δ} (a), TiO₂-200 (b), and TiO₂-400 (c); (d) cycling performance at 1 C; (e) rate capability; (f) electrochemical impedance spectroscopy over the frequency range from 100 kHz to 10 mHz.

and can be attributed to the much broader Li⁺ insertion potential range in amorphous structures.^{20,33} On the contrary, discharge–charge plateaus exist in the case of TiO₂-400, suggesting a prominent amorphous-to-crystalline phase transformation. The voltage profile plateaus in Figure 4c are a typical feature of diffusion-controlled charge storage of battery materials. Noteworthy, all three samples show high initial discharge capacities but relatively low charge capacities. The irreversible capacity loss can be ascribed to the parasitic reactions between the electrode and electrolyte resulting from the disordered structure and surface defects.⁷ Moreover, the cycling performance (Figure 4d) reveals that the capacities of both TiO_{2-δ} and TiO₂-200 undergo a self-improving process until the 20th cycle. The main reason is the electrochemical-driven phase transformation that enhances the Li⁺ transport kinetics and the gradual opening of multiple windings³⁴ in the first several cycles that efficiently augments the surface area accessible to the electrolyte and increases the reversible

adsorption/desorption of Li⁺ on the exposed amorphous TiO₂ surfaces. Owing to the stable crystalline surfaces, the reversible adsorption/desorption of Li⁺ on the exposed TiO₂-400 nanomembranes is limited, and therefore the self-improving is negligible. After 100 cycles, the reversible capacities of TiO_{2-δ} and TiO₂-200 are 195 and 184 mAh g⁻¹, respectively, both with high capacity retention of 100% (versus the 20th cycle). The highest capacity of TiO_{2-δ} is related to both the existence of Ti³⁺ and the amorphous structure, which offer more lithium storage sites and enable fast Li⁺ diffusion.^{14,35} Both amorphous TiO_{2-δ} and TiO₂-200 deliver capacity significantly higher than that of anatase TiO₂-400. This improvement can be attributed to the enhanced pseudocapacitive contributions enabled by the disordered structure, which will be discussed later.

The rate capabilities of TiO_{2-δ}, TiO₂-200, and TiO₂-400 nanomembranes are further compared in Figure 4e, which were recorded after 100 cycles at 1 C. In addition to the highest

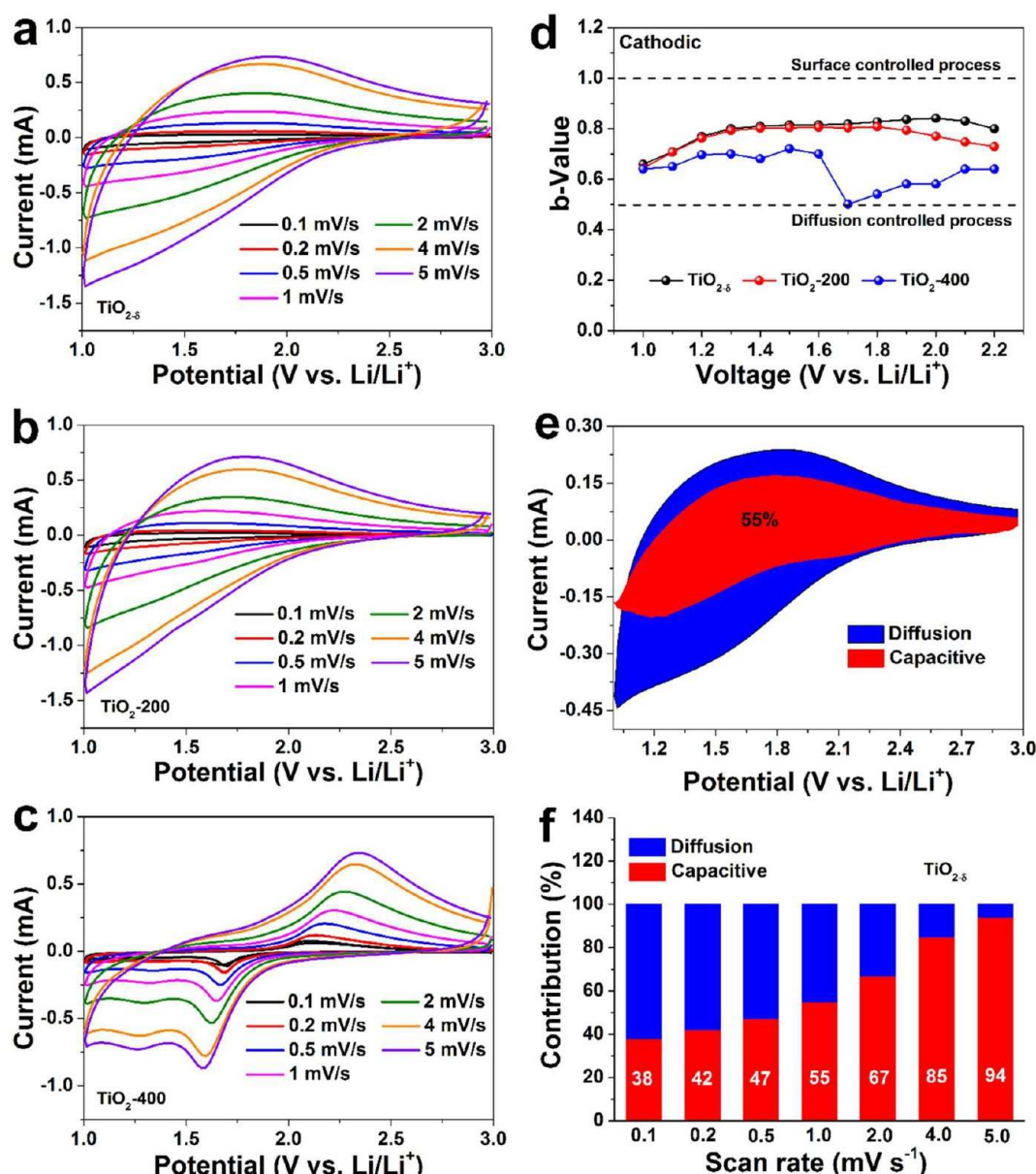


Figure 5. Kinetic analysis of the electrochemical behaviors of $\text{TiO}_{2-\delta}$, TiO_{2-200} , and TiO_{2-400} : cyclic voltammetry (CV) curves from 0.1 to 5 mV s^{-1} of $\text{TiO}_{2-\delta}$ (a), TiO_{2-200} (b), and TiO_{2-400} (c). (d) b -value determinations at different potentials for cathodic sweep. (e) Capacitive (red) and diffusion-controlled (blue) contribution of $\text{TiO}_{2-\delta}$ to the total charge storage at 1 mV s^{-1} . (f) Normalized contribution ratio ($\text{TiO}_{2-\delta}$) of capacitive (red) and diffusion-controlled (blue) capacities at different rates. At a high rate of 5 mV s^{-1} , the capacitive contribution of $\text{TiO}_{2-\delta}$ is as high as 94%.

capacity, $\text{TiO}_{2-\delta}$ nanomembranes also exhibit the best rate capability: 195 mAh g^{-1} (1 C), 170 mAh g^{-1} (2 C), 136 mAh g^{-1} (5 C), 107 mAh g^{-1} (10 C), 77 mAh g^{-1} (20 C), 61 mAh g^{-1} (30 C), 50 mAh g^{-1} (40 C), and 42 mAh g^{-1} (50 C). The higher capacities of $\text{TiO}_{2-\delta}$ at various rates than those of TiO_{2-200} provide strong evidence that the self-doped Ti^{3+} is favorable for the improvement of rate capability. Moreover, in contrast to the crystalline TiO_{2-400} , the amorphous $\text{TiO}_{2-\delta}$ and TiO_{2-200} deliver better rate capability, confirming that the amorphous feature is beneficial for fast lithium storage.

To gain further insights into the rate performances, electrochemical impedance spectroscopy (EIS) results of the $\text{TiO}_{2-\delta}$, TiO_{2-200} , and TiO_{2-400} electrodes are recorded after 10 cycles in the frequency range from 100 kHz to 10 mHz (Figure 4f). In the Nyquist plots, the semicircle in the medium-

frequency region corresponds to the charge transfer resistance (R_{ct}) at the electrode–electrolyte interface, and the inclined line in the low-frequency region represents the Warburg impedance (Z_w) associated with Li^+ diffusion in the solid phase. It can be seen that the $\text{TiO}_{2-\delta}$ shows charge transfer resistance R_{ct} lower than that of TiO_{2-200} , indicating that Ti^{3+} in the pristine sample enables faster charge transport. It should be noted that although the anatase TiO_{2-400} sample delivers a lower capacity than the amorphous TiO_2 , it exhibits the smallest charge transfer resistance R_{ct} among the three samples, suggesting that the crystalline TiO_2 has better charge transfer capability than the amorphous ones.³³ Nevertheless, the amorphous $\text{TiO}_{2-\delta}$ and TiO_{2-200} show higher Li^+ diffusion coefficients than that of the anatase TiO_{2-400} sample, as depicted in Figure S7. The easy accessibility of Li^+ in

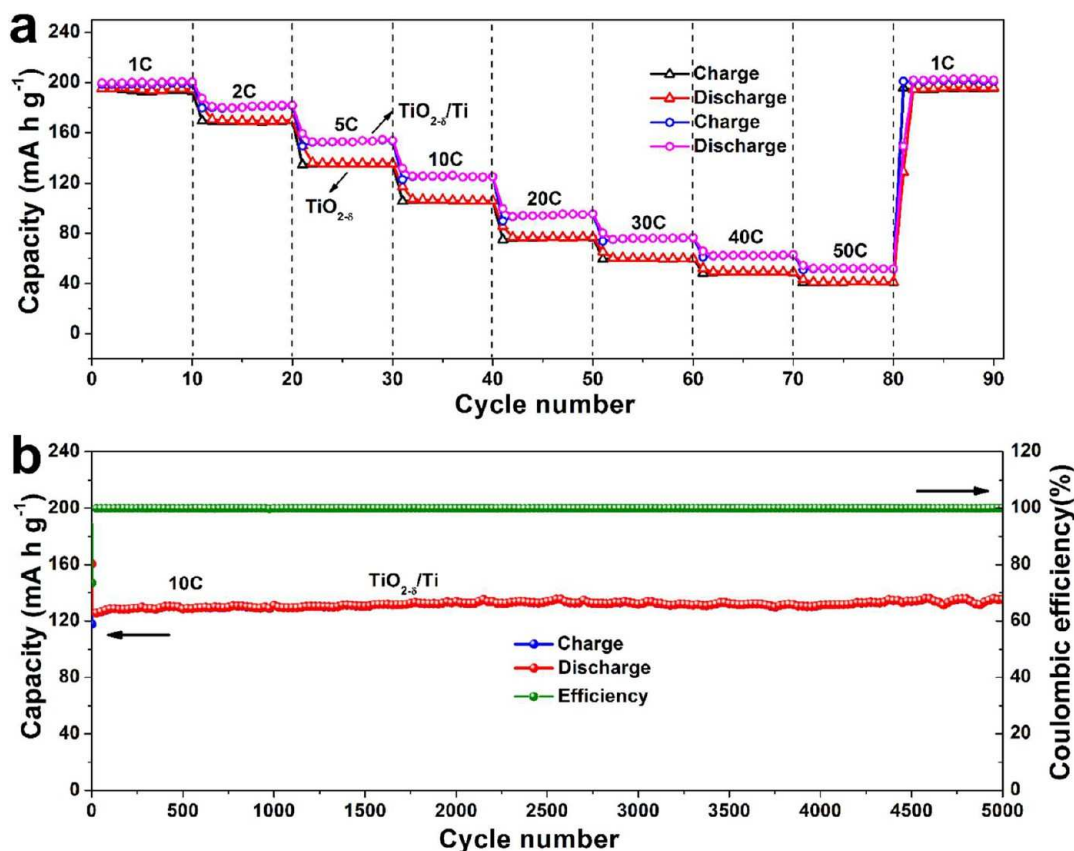


Figure 6. Electrochemical performances of TiO_{2-x} and TiO_{2-x}/Ti nanomembranes: (a) rate capabilities at various rates (recorded after cycling for 100 cycles at 1 C); (b) ultrastable performance of TiO_{2-x}/Ti nanomembranes at 10 C over 5000 cycles. No appreciable degradation in capacity is observed.

amorphous TiO₂ is due to the disordered atomic arrangements, which offer a more open framework to facilitate the ion transport.³⁴

From the above electrochemical results and analysis, we can attribute the prominent cyclability and rate capability of the TiO_{2-x} electrode to the following reasons: (a) Considering the relatively poor modulus of rupture of bulk TiO₂, the volume change (~3.1%) would lead to structure instability during the repeated Li⁺ insertion/extraction. Therefore, the roll-up process reduces the intrinsic strain significantly, thus enhancing the materials tolerance against the stress cracking and structural instability.²³ As a result, the structural integrity of the material is retained after being discharged/charged over 100 cycles (Figure S8, Supporting Information). (b) The channels between the windings increase the electrode/electrolyte contact area and shorten the Li⁺ diffusion distance. (c) The disordered structure and defects in amorphous TiO₂ contribute additional pseudocapacitance to the total capacity, resulting in the improved capacities and Li⁺-diffusion coefficient.^{20–22} (d) The self-doped Ti³⁺ ions enhance the inherent electrical conductivity and Li⁺ diffusion ability,^{12–16} thus improving the rate capability of the electrode.

Given these analyses, our results prove that the disordering of amorphous structure is beneficial for the faradaic contribution from surface processes and results in superior lithium storage properties. To study the charge storage mechanism and pseudocapacitance contribution to the total capacity of the battery, a cyclic voltammetry (CV) test from 0.1 to 5 mV s⁻¹ is presented in Figure 5a–c. Unlike the crystalline

anatase (Figure 5c) with distinct redox peaks, the amorphous TiO_{2-x} and TiO₂₋₂₀₀ nanomembranes show only one broad anodic peak ranging from 1.25 to 2.25 V at all scan rates, and no cathodic peak is visible, which is a typical behavior of amorphous TiO₂.²² Generally, there are three charge storage components in the charge storage process:^{36,37} the diffusion-controlled faradaic contribution, the faradaic contribution from charge transfer with surface/subsurface atoms (referred to as pseudocapacitance), and the nonfaradaic contribution from the double-layer capacitance. In contrast to the traditional LIBs based on diffusion-controlled lithium intercalation processes, the amorphous TiO₂ nanomembranes provide faster mass transportation in the electrode and show enhanced surface capacitive behavior.²²

The charge storage can be characterized by studying the relationship between the current (*i*) and scan rate (*ν*) according to the power law equation:^{38,39}

$$i = a\nu^b \quad (2)$$

where *a* and *b* are fitting parameters. By plotting log(*i*) against log(*ν*), we can obtain *b*-values from the slopes. Generally, a *b*-value of 0.5 (1) indicates a diffusion (surface)-controlled lithium storage process. Figures 5d presents the *b*-values for cathodic sweep at different potentials. They clearly reveal that the TiO_{2-x} nanomembranes show similar *b*-values to those of TiO₂₋₂₀₀ (~0.83), indicating both of the amorphous samples have similar charge storage behavior; that is, the charge storage is controlled by both the surface-controlled process and diffusion-controlled process. The *b*-values for anodic sweep

also show a similar result to that for cathodic sweep (Figure S9a). The ratio of the Li^+ capacitive contribution can be further quantified by separating the current response i at a fixed potential V into capacitive effects (proportional to the scan rate ν) and diffusion-controlled reactions (proportional to the square root of the scan rate ν), according to³⁶

$$i(V) = k_1\nu + k_2\nu^{1/2} \quad (3)$$

where ν is the sweep rate. By determining both k_1 and k_2 constants, we can distinguish the fraction of the current arising from Li^+ diffusion and that from capacitive processes. From the quantitative analysis, the surface capacitive contributions of $\text{TiO}_{2-\delta}$ and TiO_{2-200} electrodes at 1 mV s^{-1} are around 55% and 52%, respectively (Figure 5e and Figure S10a). As the scan rate increases, the role of capacitive contribution of the $\text{TiO}_{2-\delta}$ sample further enlarges, with a maximum value of 94% at 5 mV s^{-1} (Figure 5f). The capacitive contribution of TiO_{2-200} also gradually grows as the scan rate increases, but with slightly lower values than that of $\text{TiO}_{2-\delta}$ (Figure S10b). In contrast, the b -values of anatase TiO_2 -400 significantly decrease, especially in the region of redox peaks (the diffusion process is most likely to occur in this region). Around the redox peaks region, the b -values approach 0.5, indicating that charge storage is controlled by the Li^+ diffusion process. This is further confirmed in Figure S9b, where the peak current varies linearly with the square root of the sweep rate ($b = 0.5$). According to a similar analysis, the pseudocapacitive contribution of TiO_{2-400} is much lower than that of $\text{TiO}_{2-\delta}$ nanomembranes at various scan rates (Figure S10c,d). It provides unambiguous evidence that the higher ratio of the pseudocapacitive contribution enables faster Li^+ transport, and therefore the amorphous $\text{TiO}_{2-\delta}$ and TiO_{2-200} deliver better rate capability than the anatase TiO_2 -400.

In this work, the physical vapor deposition method facilitates complex layer stacking sequences for advanced functionalities. In the following we demonstrate that the performances of amorphous $\text{TiO}_{2-\delta}$ nanomembrane anodes can be further improved by introducing a metallic Ti layer. The idea is based on the fact that metal components in the hybrid material can enhance the electrical conductivity of the overall electrode.^{40–42} A thin metallic Ti layer is deposited onto the TiO_2 layer to form the $\text{TiO}_{2-\delta}/\text{Ti}$ sample, as shown in Figure 1b. The additional Ti layer serves as a mechanically stable, electrochemically inactive, and electrically conductive 3D network to quickly transfer the generated electrons to the current collector.

The electrochemical performances of $\text{TiO}_{2-\delta}$ and $\text{TiO}_{2-\delta}/\text{Ti}$ nanomembranes are shown and compared in Figure 6. At a low rate of 1 C, the $\text{TiO}_{2-\delta}$ and $\text{TiO}_{2-\delta}/\text{Ti}$ electrodes show similar capacities (195 and 200 mAh g^{-1} , respectively, Figure S11), which are better than most of the nanostructured TiO_2 materials reported so far (Table S1). However, the $\text{TiO}_{2-\delta}/\text{Ti}$ nanomembranes exhibit better rate capability than the $\text{TiO}_{2-\delta}$ nanomembranes, as shown in Figure 6a. As for $\text{TiO}_{2-\delta}/\text{Ti}$, with a 50-fold increase in current density (from 1 to 50 C), an excellent reversible capacity of more than 50 mAh g^{-1} could still be retained. The higher capacities of $\text{TiO}_{2-\delta}/\text{Ti}$ nanomembranes at various rates provide strong evidence that the metallic Ti network is favorable for the improvement of rate capability. The better electrical conductivity of $\text{TiO}_{2-\delta}/\text{Ti}$ is also confirmed by the EIS (Figure S12), where the charge transfer resistance R_{ct} of the $\text{TiO}_{2-\delta}/\text{Ti}$ electrode is lower, again proving the better charge transfer in the electrode–electrolyte interface owing to the presence of the conductive Ti metal network. Moreover, the $\text{TiO}_{2-\delta}/\text{Ti}$ shows a higher Li^+ diffusion

coefficient than that of the $\text{TiO}_{2-\delta}$ sample, as depicted in Figure S12b. Finally, to evaluate the cyclability at high rate, we investigate the long-life cycling performance of $\text{TiO}_{2-\delta}/\text{Ti}$ nanomembranes at 10 C. As depicted in Figure 6b, the $\text{TiO}_{2-\delta}/\text{Ti}$ nanomembranes deliver a high reversible capacity of around 135 mAh g^{-1} , holding an extraordinary capacity retention of 100% after 5000 cycles. The Coulombic efficiency remains at almost 100% over the 5000 cycles.

CONCLUSIONS

We have demonstrated that $\text{TiO}_{2-\delta}$ -based nanomembranes have a great potential to address several of the long-standing challenges associated with nanostructured TiO_2 LIB anodes. A comprehensive study based on several different designs reveals the individual contributions of the controllable Ti^{3+} self-doping, the amorphous phase, and the Ti conductive network to the lithium storage properties of TiO_2 . Owing to the synergy of these design routes, the 3D Ti^{3+} -doped TiO_2 electrode shows high specific capacity, excellent rate capability, and ultralong lifetime. Moreover, an in-depth investigation on the Li^+ kinetics reveals an interesting tunable pseudocapacitive behavior in the TiO_2 -based electrode, which is highly beneficial to fast charge storage and long-term cyclability. Our work reveals the lithium storage mechanism in TiO_2 nanomembranes and offers an ideal test bed with high reproducibility and controllability for further studies.

METHODS

Preparation of $\text{TiO}_{2-\delta}$, TiO_{2-200} , and TiO_{2-400} Nanomembranes. For the fabrication of Ti^{3+} -doped TiO_2 nanomembranes, an AR-P 3510 photoresist (Allresist GmbH) was first spin-coated as a sacrificial layer onto an Al foil-coated Si substrate at 3500 rpm for 30 s and then baked at 90°C for 5 min. Subsequently, the Ti^{3+} -doped TiO_2 layer (40 nm) was deposited onto the sacrificial layer with a rate of 0.4 \AA s^{-1} by an electron beam evaporator (BOC Edwards FL400) under an oxygen background (the chamber pressure was controlled to be 1.4×10^{-4} mbar). During the deposition, pure titanium pellets (Kurt J. Lesker) were used as the source material. The thickness of the TiO_2 layer was well controlled by a quartz crystal microbalance. After the deposition, the Al foil was unwrapped from the Si substrate and immersed into acetone to remove the sacrificial layer, during which the TiO_2 nanomembranes were peeled off from the Al foil and self-rolled up into 3D microtubes. Next, the TiO_2 tubular nanomembranes were washed by 2-propanol repeatedly until the photoresist was thoroughly rinsed away. Finally, the samples were dried in a critical point dryer (Tousimis, Autosamdri-931). As control samples, TiO_{2-200} and TiO_{2-400} nanomembranes followed the same processes and then underwent a postannealing treatment in air at 200 and 400°C for 6 h, respectively.

Preparation of $\text{TiO}_{2-\delta}/\text{Ti}$ Nanomembranes. The fabrication of $\text{TiO}_{2-\delta}/\text{Ti}$ nanomembranes was similar to that of $\text{TiO}_{2-\delta}$: AR-P 3510 photoresist (Allresist GmbH) as a sacrificial layer was first spin-coated onto an Al foil-coated Si substrate. Subsequently, the TiO_2 layer (40 nm) was deposited onto the sacrificial layer with a rate of 0.4 \AA s^{-1} by an electron beam evaporator (BOC Edwards FL400) under an oxygen background (the chamber pressure was controlled to be 1.4×10^{-4} mbar). Then the metallic Ti layer (3 nm) was deposited on top of the TiO_2 layer with a rate of 0.5 \AA s^{-1} under the chamber pressure of $(1-3) \times 10^{-6}$ mbar. After the deposition, the Al foil was unwrapped from the Si substrate and immersed into acetone to remove the sacrificial layer, during which the TiO_2/Ti nanomembranes were peeled off from the Al foil and self-rolled up into 3D microtubes. Next, the TiO_2/Ti tubular nanomembranes were washed by 2-propanol repeatedly until the photoresist was thoroughly rinsed away. Finally, the samples were dried in a critical point dryer (Tousimis, Autosamdri-931).

Materials Characterization. X-ray diffraction patterns were obtained by a Philips diffractometer at 40 kV, 40 mA, with Co K α radiation ($\lambda = 1.7902 \text{ \AA}$). Raman spectroscopy measurement was carried out at room temperature, and the signals were recorded by a LabRAM HR Evolution (Horiba) using a laser with an excitation wavelength of 458 nm. The morphology of all the products was observed by using a scanning electron microscope (Zeiss DSM982, Gemini) equipped with a field-emission gun at 3 kV acceleration voltage. Energy-dispersive X-ray spectroscopy (EDS) analysis was performed by an EDAX Genesis instrument with an acceleration voltage of 30 kV. TEM, HRTEM, HAADF-STEM, and STEM-EDS were acquired on a FEI ChemiSTEM 80-200 microscope operating at 200 kV. The surface electronic state of Ti was analyzed by XPS (PHI 5600) using monochromatic Al K α X-rays (350 W) and a pass energy of 29 eV. The TG/DSC analysis of the as-fabricated materials was performed using a SENSYS duo TGA-DSC, SETARAM Instrumentation, at a temperature ramping rate of $5 \text{ }^{\circ}\text{C min}^{-1}$ in O_2 .

Electrochemical Performances. The working electrodes were fabricated by mixing TiO_2 -based nanomembranes, conductive carbon black (Timcal), and Na-alginate binder (Aldrich) in a 70:20:10 weight ratio. The slurry was coated on a copper foil (Goodfellow) and dried in a vacuum oven at $100 \text{ }^{\circ}\text{C}$ for 12 h. The average mass loading of all the active materials is around 0.5 mg cm^{-2} . Electrochemical measurements were carried out via a Swagelok-type cell using a lithium foil as the counter and reference electrodes, a 1 M solution of LiPF_6 in ethylene carbonate/diethyl carbonate/dimethyl carbonate (1:1:1 w/w/w, BASF) containing 2.0 wt % vinylene carbonate (Aldrich) as electrolyte, and glass fibers (Whatman) as separators. Prior to assembly, all the electrodes were slightly prelithiated by placing them in direct contact with Li foils wet by the electrolyte for 60 s. The cells were assembled in an argon-filled glovebox (MBraun). Cyclic voltammetry measurements were carried out with a Zahner IM6 electrochemical workstation at sweep rates ranging from 0.1 to 5 mV s^{-1} . Galvanostatic discharge/charge cycling was studied in a potential range of 1.0–3.0 V vs Li/Li^+ with a multichannel battery testing system (Arbin BT 2000). Electrochemical impedance spectra were measured with an electrochemical workstation (Autolab PGSTAT 302N) in the 100 kHz to 10 mHz frequency range.

ASSOCIATED CONTENT

Supporting Information

The Supporting Information is available free of charge on the ACS Publications website at DOI: 10.1021/acsnano.6b07274.

TG/DSC, survey scan XPS, low-magnification SEM image, overfocused TEM image, elemental mapping images, electrochemical impedance spectroscopy, *ex situ* SEM images, *b*-value determinations for anodic sweep, capacitive and diffusion-controlled contribution to the total charge storage, cycling performances (Figures S1–S12); lithium storage capacity comparison of various TiO_2 materials (Table S1) (PDF)

AUTHOR INFORMATION

Corresponding Authors

*E-mail: s.z.huang@ifw-dresden.de.

*E-mail: lin.zhang@ifw-dresden.de.

ORCID

Shaozhuan Huang: 0000-0002-4188-6421

Lifeng Liu: 0000-0003-2732-7399

Xiaolei Sun: 0000-0001-6327-1527

Notes

The authors declare no competing financial interest.

ACKNOWLEDGMENTS

We thank Bo Liu and Jinbo Pang for the fruitful discussions. This work was financially supported by the German Science Foundation (DFG) under the program “Temporary Position for Principal Investigator”.

REFERENCES

- (1) Armand, M.; Tarascon, J.-M. Building Better Batteries. *Nature* **2008**, *451*, 652–657.
- (2) Sun, Y. K.; Chen, Z.; Noh, H. J.; Lee, D. J.; Jung, H. G.; Ren, Y.; Wang, S.; Yoon, C. S.; Myung, S. T.; Amine, K. Nanostructured High-Energy Cathode Materials for Advanced Lithium Batteries. *Nat. Mater.* **2012**, *11*, 942–947.
- (3) Sun, M. H.; Huang, S. Z.; Chen, L. H.; Li, Y.; Yang, X. Y.; Yuan, Z. Y.; Su, B. L. Applications of Hierarchically Structured Porous Materials from Energy Storage and Conversion, Catalysis, Photocatalysis, Adsorption, Separation, and Sensing to Biomedicine. *Chem. Soc. Rev.* **2016**, *45*, 3479–3563.
- (4) Liu, S.; Jia, H.; Han, L.; Wang, J.; Gao, P.; Xu, D.; Yang, J.; Che, S. Nanosheet-Constructed Porous TiO_2 -B for Advanced Lithium Ion Batteries. *Adv. Mater.* **2012**, *24*, 3201–3204.
- (5) Jin, J.; Huang, S. Z.; Shu, J.; Wang, H. E.; Li, Y.; Yu, Y.; Chen, L. H.; Wang, B. J.; Su, B. L. Highly Porous TiO_2 Hollow Microspheres Constructed by Radially Oriented Nanorods Chains for High Capacity, High Rate and Long Cycle Capability Lithium Battery. *Nano Energy* **2015**, *16*, 339–349.
- (6) Jin, J.; Huang, S. Z.; Liu, J.; Li, Y.; Chen, L. H.; Yu, Y.; Wang, H. E.; Grey, C. P.; Su, B. L. Phases Hybridizing and Hierarchical Structuring of Mesoporous TiO_2 Nanowire Bundles for High-Rate and High-Capacity Lithium Batteries. *Adv. Sci.* **2015**, *2*, 1500070.
- (7) Yan, X.; Wang, Z.; He, M.; Hou, Z.; Xia, T.; Liu, G.; Chen, X. TiO_2 Nanomaterials as Anode Materials for Lithium-Ion Rechargeable Batteries. *Energy Technol.* **2015**, *3*, 801–814.
- (8) Zhang, K.; Katz, M. B.; Li, B.; Kim, S. J.; Du, X.; Hao, X.; Jokisaari, J. R.; Zhang, S.; Graham, G. W.; Van der Ven, A. Water-Free Titania-Bronze Thin Films with Superfast Lithium-Ion Transport. *Adv. Mater.* **2014**, *26*, 7365–7370.
- (9) Liu, L.; Fan, Q.; Sun, C.; Gu, X.; Li, H.; Gao, F.; Chen, Y.; Dong, L. Synthesis of Sandwich-like TiO_2 @C Composite Hollow Spheres with High Rate Capability and Stability for Lithium-Ion Batteries. *J. Power Sources* **2013**, *221*, 141–148.
- (10) Tan, L.; Pan, L.; Cao, C.; Wang, B.; Li, L. Nitrogen-Doped Carbon Coated TiO_2 Nanocomposites as Anode Material to Improve Cycle Life for Lithium-Ion Batteries. *J. Power Sources* **2014**, *253*, 193–200.
- (11) Asahi, R.; Morikawa, T.; Ohwaki, T.; Aoki, K.; Taga, Y. Visible-Light Photocatalysis in Nitrogen-Doped Titanium Oxides. *Science* **2001**, *293*, 269–271.
- (12) Naldoni, A.; Allietta, M.; Santangelo, S.; Marelli, M.; Fabbri, F.; Cappelli, S.; Bianchi, C. L.; Psaro, R.; Dal Santo, V. Effect of Nature and Location of Defects on Bandgap Narrowing in Black TiO_2 Nanoparticles. *J. Am. Chem. Soc.* **2012**, *134*, 7600–7603.
- (13) Chen, X.; Liu, L.; Huang, F. Black titanium Dioxide (TiO_2) Nanomaterials. *Chem. Soc. Rev.* **2015**, *44*, 1861–1885.
- (14) Shin, J.-Y.; Joo, J. H.; Samuelis, D.; Maier, J. Oxygen-Deficient TiO_{2-x} Nanoparticles via Hydrogen Reduction for High Rate Capability Lithium Batteries. *Chem. Mater.* **2012**, *24*, 543–551.
- (15) Myung, S.-T.; Kikuchi, M.; Yoon, C. S.; Yashiro, H.; Kim, S.-J.; Sun, Y.-K.; Scrosati, B. Black Anatase Titania Enabling Ultra High Cycling Rates for Rechargeable Lithium Batteries. *Energy Environ. Sci.* **2013**, *6*, 2609–2614.
- (16) Chen, J.; Song, W.; Hou, H.; Zhang, Y.; Jing, M.; Jia, X.; Ji, X. Ti^{3+} Self-Doped Dark Rutile TiO_2 Ultrafine Nanorods with Durable High-Rate Capability for Lithium-Ion Batteries. *Adv. Funct. Mater.* **2015**, *25*, 6793–6801.
- (17) Gao, X.; Li, G.; Xu, Y.; Hong, Z.; Liang, C.; Lin, Z. TiO_2 Microboxes with Controlled Internal Porosity for High-Performance Lithium Storage. *Angew. Chem., Int. Ed.* **2015**, *54*, 14331–14335.

- (18) Schmidt, O. G.; Eberl, K. Nanotechnology: Thin Solid Films Roll Up into Nanotubes. *Nature* **2001**, *410*, 168–168.
- (19) Legrain, F.; Malyi, O.; Manzhos, S. Insertion Energetics of Lithium, Sodium, and Magnesium in Crystalline and Amorphous Titanium Dioxide: A Comparative First-Principles Study. *J. Power Sources* **2015**, *278*, 197–202.
- (20) Fang, H. T.; Liu, M.; Wang, D. W.; Sun, T.; Guan, D. S.; Li, F.; Zhou, J.; Sham, T. K.; Cheng, H. M. Comparison of the Rate Capability of Nanostructured Amorphous and Anatase TiO₂ for Lithium Insertion Using Anodic TiO₂ Nanotube Arrays. *Nanotechnology* **2009**, *20*, 225701.
- (21) Ban, C.; Xie, M.; Sun, X.; Travis, J. J.; Wang, G.; Sun, H.; Dillon, A. C.; Lian, J.; George, S. M. Atomic Layer Deposition of Amorphous TiO₂ on Graphene as an Anode for Li-Ion Batteries. *Nanotechnology* **2013**, *24*, 424002.
- (22) Li, S.; Xue, P.; Lai, C.; Qiu, J.; Ling, M.; Zhang, S. Pseudocapacitance of Amorphous TiO₂@Nitrogen Doped Graphene Composite for High Rate Lithium Storage. *Electrochim. Acta* **2015**, *180*, 112–119.
- (23) Deng, J.; Ji, H.; Yan, C.; Zhang, J.; Si, W.; Baunack, S.; Oswald, S.; Mei, Y.; Schmidt, O. G. Naturally Rolled-up C/Si/C Trilayer Nanomembranes as Stable Anodes for Lithium-Ion Batteries with Remarkable Cycling Performance. *Angew. Chem.* **2013**, *125*, 2382–2386.
- (24) Giudicatti, S.; Marz, S. M.; Soler, L.; Madani, A.; Jorgensen, M. R.; Sanchez, S.; Schmidt, O. G. Photoactive Rolled-Up TiO₂ Microtubes: Fabrication, Characterization and Applications. *J. Mater. Chem. C* **2014**, *2*, 5892–5901.
- (25) Harsha, K. S. Thermal evaporation sources. In *Principles of Vapor Deposition of Thin Films*; Great Britain, 2005; p 400.
- (26) Deskins, N. A.; Rousseau, R.; Dupuis, M. Defining the Role of Excess Electrons in the Surface Chemistry of TiO₂. *J. Phys. Chem. C* **2010**, *114*, 5891–5897.
- (27) Li, G.; Lian, Z.; Li, X.; Xu, Y.; Wang, W.; Zhang, D.; Tian, F.; Li, H. Ionothermal Synthesis of Black Ti³⁺-Doped Single-Crystal TiO₂ as an Active Photocatalyst for Pollutant Degradation and H₂ Generation. *J. Mater. Chem. A* **2015**, *3*, 3748–3756.
- (28) Li, K.; Gao, S.; Wang, Q.; Xu, H.; Wang, Z.; Huang, B.; Dai, Y.; Lu, J. In-Situ-Reduced Synthesis of Ti³⁺ Self-Doped TiO₂/G-C₃N₄ Heterojunctions with High Photocatalytic Performance Under Led Light Irradiation. *ACS Appl. Mater. Interfaces* **2015**, *7*, 9023–9030.
- (29) Wu, L.; Bresser, D.; Buchholz, D.; Giffin, G. A.; Castro, C. R.; Ochel, A.; Passerini, S. Unfolding the Mechanism of Sodium Insertion in Anatase TiO₂ Nanoparticles. *Adv. Energy Mater.* **2015**, *5*, 1401142.
- (30) Lee, W.; Scholz, R.; Gösele, U. A Continuous Process for Structurally Well-Defined Al₂O₃ Nanotubes Based on Pulse Anodization of Aluminum. *Nano Lett.* **2008**, *8*, 2155–2160.
- (31) Zhu, G. N.; Wang, Y. G.; Xia, Y. Y. Ti-based Compounds as Anode Materials for Li-Ion Batteries. *Energy Environ. Sci.* **2012**, *5*, 6652–6667.
- (32) Reddy, M.; Subba Rao, G.; Chowdari, B. Metal Oxides and Oxyalts as Anode Materials for Li Ion Batteries. *Chem. Rev.* **2013**, *113*, 5364–5457.
- (33) Huang, S. Z.; Cai, Y.; Jin, J.; Li, Y.; Zheng, X. F.; Wang, H. E.; Wu, M.; Chen, L. H.; Su, B. L. Annealed Vanadium Oxide Nanowires and Nanotubes as High Performance Cathode Materials for Lithium Ion Batteries. *J. Mater. Chem. A* **2014**, *2*, 14099–14108.
- (34) Zhou, M.; Xu, Y.; Xiang, J.; Wang, C.; Liang, L.; Wen, L.; Fang, Y.; Mi, Y.; Lei, Y. Understanding the Orderliness of Atomic Arrangement toward Enhanced Sodium Storage. *Adv. Energy Mater.* **2016**, *6*, 1600448.
- (35) Fan, L. Z.; Chi, S. S.; Wang, L. N.; Song, W. L.; He, M.; Gu, L. Synthesis of TiO_x Nanotubular Arrays with Oxygen Defects as High-Performance Anodes for Lithium-Ion Batteries. *ChemElectroChem* **2015**, *2*, 421–426.
- (36) Brezesinski, T.; Wang, J.; Tolbert, S. H.; Dunn, B. Ordered Mesoporous [alpha]-MoO₃ with Iso-Oriented Nanocrystalline Walls for Thin-Film Pseudocapacitors. *Nat. Mater.* **2010**, *9*, 146–151.
- (37) Chao, D.; Zhu, C.; Yang, P.; Xia, X.; Liu, J.; Wang, J.; Fan, X.; Savilov, S. V.; Lin, J.; Fan, H. J. Array of Nanosheets Render Ultrafast and High-Capacity Na-Ion Storage by Tunable Pseudocapacitance. *Nat. Commun.* **2016**, *7*, 12122.
- (38) Augustyn, V.; Come, J.; Lowe, M. A.; Kim, J. W.; Taberna, P. L.; Tolbert, S. H.; Abruna, H. D.; Simon, P.; Dunn, B. High-Rate Electrochemical Energy Storage through Li⁺ Intercalation Pseudocapacitance. *Nat. Mater.* **2013**, *12*, 518–522.
- (39) Augustyn, V.; Simon, P.; Dunn, B. Pseudocapacitive Oxide Materials for High-Rate Electrochemical Energy Storage. *Energy Environ. Sci.* **2014**, *7*, 1597–1614.
- (40) Deng, J.; Yan, C.; Yang, L.; Baunack, S.; Oswald, S.; Wendrock, H.; Mei, Y.; Schmidt, O. G. Sandwich-Stacked SnO₂/Cu Hybrid Nanosheets as Multichannel Anodes for Lithium Ion Batteries. *ACS Nano* **2013**, *7*, 6948–6954.
- (41) Yan, C.; Xi, W.; Si, W.; Deng, J.; Schmidt, O. G. Highly Conductive and Strain-Released Hybrid Multilayer Ge/Ti Nanomembranes with Enhanced Lithium-Ion-Storage Capability. *Adv. Mater.* **2013**, *25*, 539–544.
- (42) Yu, Y.; Gu, L.; Lang, X.; Zhu, C.; Fujita, T.; Chen, M.; Maier, J. Li Storage in 3D Nanoporous Au-Supported Nanocrystalline Tin. *Adv. Mater.* **2011**, *23*, 2443–2447.